Available online at www.sciencedirect.com
ScienceDirect
International Journal of Solids and Structures 44 (2007) 1438–1460
INTERNATIONAL JOURNAL OF SOLIDS and STRUCTURES
www.elsevier.com/locate/ijsolstr

A Reissner–Mindlin limit analysis model for out-of-plane loaded running bond masonry walls

A. Cecchi [a], G. Milani [b,*], A. Tralli [b]

[a] *IUAV University of Venice, Dorsoduro 2206, ex convento Terese, 30123 Venice, Italy*
[b] *Department of Engineering, University of Ferrara, Via Saragat 1, 44100 Ferrara, Italy*

Received 5 April 2006; received in revised form 29 May 2006
Available online 27 June 2006

Abstract

Earthquake surveys have demonstrated that the lack of out-of-plane strength is a primary cause of failure in many traditional forms of masonry. Moreover, bearing walls are relatively thick and, as a matter of fact, many codes of practice impose a minimal slenderness for them, as for instance the recent Italian O.P.C.M. 3431 [2005. Ulteriori modifiche ed integrazioni all'OPCM 3274/03 (in Italian) and O.P.C.M. 3274, 20/03/2003, Primi elementi in materia di criteri generali per la classificazione sismica del territorio nazionale e di normative tecniche per le costruzioni in zona sismica (in Italian)], in which the upper bound slenderness is fixed respectively equal to 12 for artificial bricks and 10 for natural blocks masonry. In this context, a formulation at failure for regular assemblages of bricks based both on homogenization and Reissner–Mindlin theory seems particularly attractive. In this paper a kinematic limit analysis approach under the hypotheses of the thick plate theory is developed for the derivation of the macroscopic failure surfaces of masonry out-of-plane loaded. The behavior of a 3D system of blocks connected by interfaces is identified with a 2D Reissner–Mindlin plate. Infinitely resistant blocks connected by interfaces (joints) with a Mohr–Coulomb failure criterion with tension cut-off and compressive cap are considered. Finally, an associated flow rule for joints is adopted. In this way, the macroscopic masonry failure surface is obtained as a function of the macroscopic bending moments, torsional moments and shear forces by means of a linear programming problem in which the internal power dissipated is minimized, once that a subclass of possible deformation modes is a priori chosen. Several examples of technical relevance are presented and comparisons with previously developed Kirchhoff–Love static [Milani, G., Lourenço, P.B., Tralli, A., 2006b. A homogenization approach for the limit analysis of out-of-plane loaded masonry walls. J. Struct. Eng. ASCE (in press)] and kinematic [Sab, K., 2003.Yield design of thin periodic plates by a homogenisation technique and an application to masonry walls. C.R. Mech. 331, 641–646] failure surfaces are provided. Finally, two meaningful structural examples are reported, the first concerning a masonry wall under cylindrical flexion, the second consisting of a rectangular plate with a central opening out-of-plane loaded. For both cases, the influence of the shear strength on the collapse load is estimated.

Keywords: Masonry; Reissner–Mindlin plates; Limit analysis; Out-of-plane loads

* Corresponding author. Tel.: +39 0532 974911; fax: +39 0532 974870.
E-mail addresses: gmilani@ing.unife.it, gabriele.milani@unife.it (G. Milani).

0020-7683/$ - see front matter © 2006 Elsevier Ltd. All rights reserved.
doi:10.1016/j.ijsolstr.2006.06.033

1. Introduction

The prediction of the ultimate load bearing capacity of masonry walls out-of-plane loaded is of great relevance for the design of masonry structures. Out-of-plane failures are mostly related to seismic and wind loads and the lack of out-of-plane strength is a primary cause of failure in different forms of masonry, particularly in the case of historical buildings (see for instance Spence and Coburn, 1992). Furthermore, masonry structures are often subjected simultaneously to in-plane compressive vertical loads (either self weight and permanent loads) and out-of-plane actions. Vertical loads increase both the ultimate out-of-plane strength and the ductility of masonry, and bring additional complexity to the structural analysis.

Laboratory tests conducted by Gazzola et al. (1985) and Southcombe et al. (1995) on brick masonry walls subjected to lateral loads have shown both that failure takes place along a well-defined pattern of lines and that, in many cases, fractures take place at the interface between bricks and mortar.

On the other hand, limit analysis approaches have been widely used for the analysis at failure of masonry structures, because they require only a reduced number of material parameters and provide limit multipliers of loads, failure mechanisms and, at least on critical sections, the stress distribution at collapse (see Sutcliffe et al., 2001). Furthermore, masonry presents a very limited tensile strength and, as a first attempt, this suggested the extension of limit analysis theorems to no-tension materials (see Del Piero, 1998).

Moreover, other distinctive aspects of masonry at failure should be considered, such as its anisotropy (Milani et al., 2006a), closely related to the constituent materials (mortar and units) and to the bond pattern, and its limited compressive strength, as demonstrated experimentally by Page (1981) for in-plane biaxial compression tests.

Furthermore, an adding important phenomenological aspect that should be considered is that bearing walls are relatively thick. Many codes of practice require for them a minimal slenderness ratio λ, as for instance the recent Italian code O.P.C.M. 3431 (2005), in which an upper bound equal to 12 for artificial bricks and 10 for natural blocks masonry is imposed for λ.

In this framework, a kinematic limit analysis approach in which $(-a)$ bricks are supposed infinitely resistant and $(-b)$ joints are reduced to interfaces may be used in order to have a realistic prediction of the actual behavior at failure of panels out-of-plane loaded.

Approaches based on the classic homogenization theory have been presented under these hypotheses by de Buhan and de Felice (1997) for in-plane loaded walls and by Sab (2003) for out-of-plane loaded thin plates. In both cases, a classic Mohr–Coulomb failure criterion obeying an associated flow rule for joints was adopted.

It is worth mentioning that frictional phenomena may require the adoption of non-associated flow rules for the constituent materials (see for instance Ferris and Tin-Loi, 2001; Orduña and Lourenço, 2005). Such non-standard materials were studied since the early limit analysis development stages (Palmer, 1966). More recent investigations can be found in Corigliano and Maier (1995) and De Saxcé and Bousshine (1998). As a matter of fact, this hypothesis implies the lack of the uniqueness of the solution, i.e. that a multiplicity of solutions can exist for these limit analysis problems (see Begg and Fishwick, 1995, where a formulation for non-associated limit analysis of two-dimensional voussoir arches is presented).

For this reason, in the framework of classic limit analysis theorems, here an associated flow rule is adopted for joints. This leads to treat simple linear programming problems, which can be solved easily by means of standard packages.

In this paper, a simplified micro-mechanical model is developed for the kinematic limit analysis of masonry walls under Reissner–Mindlin plate hypotheses.

Masonry skeleton is represented by a 3D discrete system of blocks interacting through interfaces (the mortar joints). Blocks are supposed infinitely resistant, whereas for joints a Mohr–Coulomb failure criterion for representing frictional phenomena with tension cut-off and compressive limited strength is adopted. In this way, a full description of the model can be given considering a representative volume constituted by a generic brick with its 6 neighbors. In order to obtain a Reissner–Mindlin equivalent plate, a sub-class of motions for the representative volume is a priori assumed, so that horizontal and vertical flexion and torsion are reproduced, as well as out-of-plane sliding, as a consequence of the Reissner–Mindlin model assumed.

Then, a numerical procedure of identification between the 3D discrete Lagrangian system and a continuum equivalent model is implemented. Such identification is based on a simple correspondence between motions in the 3D discrete model and the continuum.

It is worth noting that in the limit analysis model proposed, which requires a C^0 continuity of the displacements field in the elastic range, discontinuous velocity fields can be assumed at the interfaces between adjacent blocks, so allowing an accurate description of the actual out-of-plane failure mechanisms, mainly concentrated at the bond between mortar and bricks.

Since internal dissipation can take place only at the interface between bricks, a simple constrained minimization problem in few variables is obtained. Macroscopic masonry failure surfaces are numerically evaluated as a function of the macroscopic bending and torsional moments and out-of-plane shear forces.

In Section 2, the basic assumptions adopted for the identification model are presented, whereas in Section 3 the constrained minimization problem for obtaining macroscopic failure surfaces for masonry is reported.

In Section 4, the micro-mechanical model is applied for some cases of technical interest for the evaluation of the out-of-plane macroscopic failure surfaces of masonry. Several cases are reported and validated, where possible, against closed-form solutions recently presented. Finally, in Section 5 two structural examples are discussed, the first concerning a masonry wall under cylindrical flexion, the second consisting of a rectangular plate with a central opening out-of-plane loaded. For both cases, the influence of the shear strength on the collapse load is estimated.

2. Basic assumptions

In this section, a procedure to build a Reissner–Mindlin plate model based on a correspondence between equivalent class of motions in a 3D discrete blocks system and a plate continuous model is presented.

The two models are described separately and then an equivalence procedure between the kinematic descriptors in the two systems is performed, in order to study masonry as a 2D thick plate. It worth mentioning that the basic idea of this approach may be found in a classical Hill's paper (Hill, 1965). It is worth noting that the formulation of the model does not impose a field local solution as, for instance, occurs using standard homogenization procedures, but imposes only a kinematic correspondence between motions. This assumption implies that the obtained solution is kinematically admissible.

2.1. Kinematics

Masonry is represented by infinitely resistant blocks connected by mortar joints reduced to interfaces with rigid-plastic behavior (Fig. 1). The motion of a generic block $\mathscr{A}$ may be described as a function of its center velocity $\mathbf{w}^a$ and its angular velocity $\mathbf{\Omega}^a$. Starting from this assumption, the motions of all the blocks in contact to block $\mathscr{A}$ may be described. Hence, to describe the kinematic model at hand is sufficient to take into consideration the interaction of a generic couple of blocks, $(\mathscr{A}, \mathscr{B})$.

Let $\mathbf{p}$ be the center of the I interface between $\mathscr{A}$ and $\mathscr{B}$. The velocity of the material points $\mathbf{x}$ of $\mathscr{A}$ and $\mathscr{B}$ in contact in a position $\xi \in I$ may be written as:

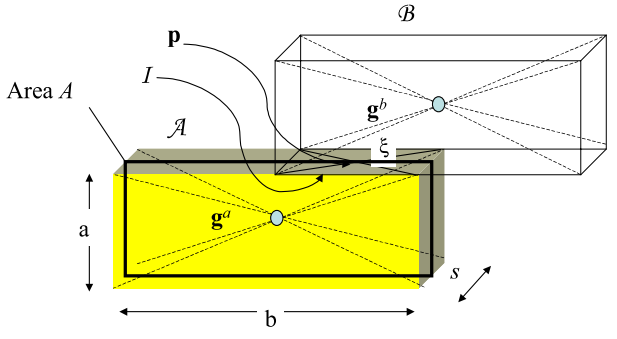

Fig. 1. Geometrical description of the model; two adjacent bricks ($\mathbf{g}^a$ and $\mathbf{g}^b$) connected with a mortar interface I where plastic dissipation occurs.

$$\begin{aligned}\mathbf{w}^a(\mathbf{x}) &= \mathbf{w}^a(\mathbf{p}) + \boldsymbol{\Omega}^a(\boldsymbol{\xi} - \mathbf{p})\\ \mathbf{w}^b(\mathbf{x}) &= \mathbf{w}^b(\mathbf{p}) + \boldsymbol{\Omega}^b(\boldsymbol{\xi} - \mathbf{p}).\end{aligned} \tag{1}$$

The jump of the velocity field $\mathbf{w}(\boldsymbol{\xi})$ between $\mathscr{A}$ and $\mathscr{B}$ in a point $\boldsymbol{\xi} \in I$ can be written as:

$$\lfloor \mathbf{w}(\boldsymbol{\xi}) \rfloor = \mathbf{w}^b(\boldsymbol{\xi}) - \mathbf{w}^a(\boldsymbol{\xi}) = \mathbf{w}^b(\mathbf{p}) - \mathbf{w}^{\mathbf{a}}(\mathbf{p}) + \boldsymbol{\Omega}^{\mathbf{b}}(\boldsymbol{\xi} - \mathbf{p}) - \boldsymbol{\Omega}^{\mathbf{a}}(\boldsymbol{\xi} - \mathbf{p}) = \mathbf{w}_{\mathbf{p}} + \boldsymbol{\Omega}_{\mathbf{p}}(\boldsymbol{\xi} - \mathbf{p}) \tag{2}$$

where $\mathbf{w}_p = \mathbf{w}^b(\mathbf{p}) - \mathbf{w}^a(\mathbf{p})$ and $\boldsymbol{\Omega}_p = \boldsymbol{\Omega}^b - \boldsymbol{\Omega}^a$.

On the other hand, fields $\mathbf{t}^a(\boldsymbol{\xi})$ and $\mathbf{t}^b(\boldsymbol{\xi})$ for $\boldsymbol{\xi} \in I$ can be introduced, representing the contact forces between blocks $\mathscr{A}$ and $\mathscr{B}$. Equilibrium conditions require that $\mathbf{t}^a(\boldsymbol{\xi}) = -\mathbf{t}^b(\boldsymbol{\xi})$. Hence, it is possible to define the power-set $\mathbf{t}^b(\boldsymbol{\xi}) = \mathbf{t}(\boldsymbol{\xi})$-dissipated at the interface as follows:

$$\pi = \int_I \mathbf{t}^a(\boldsymbol{\xi}) \cdot \mathbf{w}^a(\boldsymbol{\xi}) + \mathbf{t}^b(\boldsymbol{\xi}) \cdot \mathbf{w}^b(\boldsymbol{\xi}) = \int_I \mathbf{t}(\boldsymbol{\xi}) \cdot [\mathbf{w}^b(\boldsymbol{\xi}) - \mathbf{w}^a(\boldsymbol{\xi})] = \mathbf{t}_p \cdot \mathbf{w}_p + \boldsymbol{\Omega}_p \cdot \int_I \operatorname{skw} \mathbf{t} \otimes (\boldsymbol{\xi} - \mathbf{p}). \tag{3}$$

Denoting with $\mathbf{t}_p = \int_I \mathbf{t}(\boldsymbol{\xi})$ and with $\mathbf{M}_p = 2\int_I \operatorname{skw} \mathbf{t} \otimes (\boldsymbol{\xi} - \mathbf{p})$, the power dissipated reported in Eq. (3) can be written as follows:

$$\pi_p = \mathbf{t}_p \cdot \mathbf{w}_p + \frac{1}{2}\mathbf{M}_p \cdot \boldsymbol{\Omega}_p. \tag{4}$$

2.2. Reissner–Mindlin continuous plate model

In this section, a 2D plate model is introduced independently from the discrete 3D model previously discussed. Here, the term plate is used to describe a bi-dimensional continuum, identified by its middle plane S of normal $\mathbf{e}_3$ (Fig. 2).

A generic motion in a plate continuum model is described by the following fields:

$$\begin{aligned}&\mathbf{w}(\mathbf{x})\\ &\boldsymbol{\Omega}(\mathbf{x})\end{aligned} \tag{5}$$

where $\mathbf{w}(\mathbf{x})$ and $\boldsymbol{\Omega}(\mathbf{x})$ are the velocity vector and angular velocity tensor of the material point $\mathbf{x}$, respectively.

As well known, in the case of both in- and out-of-plane loads, internal forces tensor $\mathbf{N}$ (membrane and shear) and bending and torsion moments tensor $\mathbf{M}$ are introduced.

Consequently, the mechanical power evaluated on S may be written as:

$$\pi = \mathbf{N} \cdot \operatorname{sym}(\operatorname{grad} \mathbf{w}) + (\mathbf{N}\mathbf{e}_3 \otimes \mathbf{e}_3) \cdot \boldsymbol{\Omega} + \mathbf{M} \cdot \operatorname{sym}(\operatorname{grad} \boldsymbol{\Omega}\mathbf{e}_3) \tag{6}$$

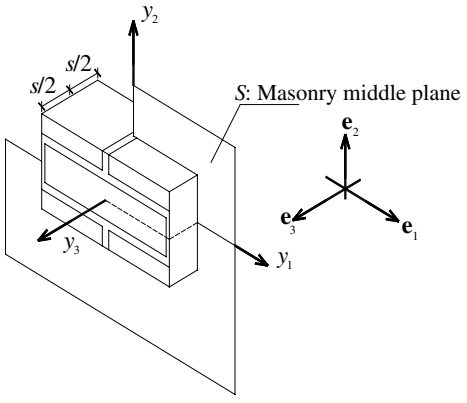

Fig. 2. Reference surface chosen for masonry.

where grad represents the gradient operator on S. Total internal power dissipated can be evaluated as the sum of power dissipated by membrane actions, plate shear actions, bending and torsional moments. In particular, by indicating with an upper line the projection on S, the previous equation becomes:

$$\pi = \overline{\mathbf{N}} \cdot \mathrm{sym}(\mathrm{grad}\,\bar{\mathbf{w}}) + \mathbf{T} \cdot (\mathrm{grad}\, w_3 + \boldsymbol{\Omega}\mathbf{e}_3) + \mathbf{M} \cdot \mathrm{sym}(\mathrm{grad}\,\boldsymbol{\Omega}\mathbf{e}_3). \tag{7}$$

In what follows we assume:

– $\mathrm{sym}(\mathrm{grad}\,\bar{\mathbf{w}}) = \dot{\mathbf{E}}$, where $\dot{\mathbf{E}}$ is the in-plane membrane strain rate tensor;
– $\mathrm{sym}(\mathrm{grad}\,\boldsymbol{\Omega}\mathbf{e_3}) = \dot{\boldsymbol{\chi}}$, where $\dot{\boldsymbol{\chi}}$ is the curvature rate tensor ($\dot{\chi}_{\alpha\beta} = 1/2(\omega_{\alpha,\beta} + \omega_{\beta,\alpha})$ with $\alpha, \beta = 1, 2$);
– $\mathrm{grad}\, w_3 + \boldsymbol{\Omega}\mathbf{e}_3 = \dot{\boldsymbol{\gamma}} = [\dot{\gamma}_{13} \;\; \dot{\gamma}_{23}]^{\mathrm{T}}$, where $\dot{\boldsymbol{\gamma}}$ is the shear strain rate vector.

Furthermore, $\overline{\mathbf{N}}$ represents the membrane actions tensor, $\mathbf{N}\mathbf{e}_3 = \mathbf{T}$ represents the shear actions vector and $\mathbf{M}$ represents the bending moments and torsion tensor. It must be noted that the angular velocity tensor $\boldsymbol{\Omega}(\mathbf{x})$ in the case of a plate model is:

$$\boldsymbol{\Omega} = \begin{pmatrix} 0 & 0 & \omega_2 \\ 0 & 0 & -\omega_1 \\ -\omega_2 & \omega_1 & 0 \end{pmatrix} \tag{8}$$

with ω_3 component equal to zero.

2.3. Compatible equivalent model

A portion of a $\mathscr{P}$ masonry panel with the same dimensions of the REV is considered. This portion is chosen so that its center $\mathbf{g}^a$ coincides with the center of block $\mathscr{A}$. A portion of plate $\mathscr{H}$, with the same edge is considered, so that the $\mathbf{x}$ point of $\mathscr{H}$ coincides with $\mathbf{g}^a$ (Fig. 3).

Afterwards, a correspondence between a class of regular motions in $\mathscr{P}$ and $\mathscr{H}$ is assigned:

$$\begin{aligned} \mathbf{w}^a &= \mathbf{w}(\mathbf{x}) \\ \boldsymbol{\Omega}^a &= \boldsymbol{\Omega}(\mathbf{x}) \end{aligned} \tag{9}$$

and

$$\begin{aligned} \mathbf{w}^b(\mathbf{x}) &= \mathbf{w}(\mathbf{x}) + \mathrm{grad}\,\mathbf{w}(\mathbf{x})(\mathbf{g}^b - \mathbf{x}) \\ \boldsymbol{\Omega}^b(\mathbf{x}) &= \boldsymbol{\Omega}(\mathbf{x}) + \mathrm{grad}\,\boldsymbol{\Omega}(\mathbf{x})(\mathbf{g}^b - \mathbf{x}) \end{aligned} \tag{10}$$

where $\mathbf{g}^b$ is the center of a $\mathscr{B} \in \mathscr{P}$ generic brick. Eq. (9) imposes that velocity and angular velocity of the center of the brick $\mathscr{A}$ in the discrete system and velocity and angular velocity of the center of the REV in the

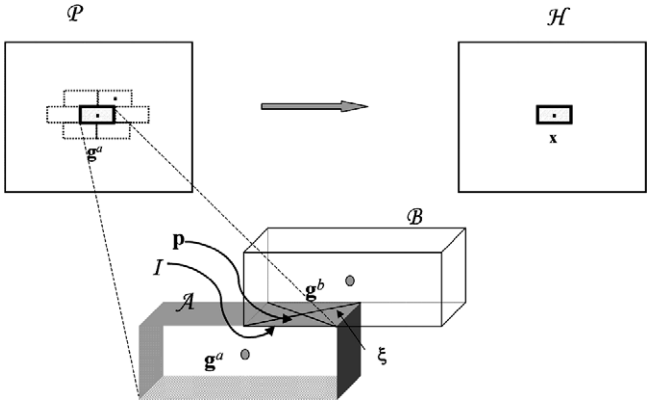

Fig. 3. Representative volume element and identification between discrete model and continuous model.

continuum model are equal. Moreover, in (10) the velocity and angular velocity of the center of the brick $\mathscr{B}$ in the discrete system correspond to a first order Taylor approximation (first order identification) in the velocity and angular velocity in the continuum model, respectively.

Let us define the vector $\mathbf{t}_p$ as $\mathbf{t}_p = \bar{\mathbf{t}}_p + \mathbf{t}_{3p} = [t_{1p}\ \ t_{2p}\ \ 0]^{\mathrm{T}} + [0\ \ 0\ \ t_{3p}]^{\mathrm{T}}$ where $\bar{\mathbf{t}}_p$ denotes the projection on S of $\mathbf{t}_p$ and $\mathbf{t}_{3p}$ is the component orthogonal to S of $\mathbf{t}_p$. Taking into consideration correspondent motion tests, from Eqs. (9) and (10), (4) may be written as:

$$\begin{aligned}\mathbf{t}_p \cdot \mathbf{w}_p &= \bar{\mathbf{t}}_p \otimes (\mathbf{g}^b - \mathbf{g}^a) \cdot (\operatorname{grad} \bar{\mathbf{w}}) + \mathbf{t}_{3p}(\mathbf{g}^b - \mathbf{g}^a) \cdot (\operatorname{grad} w_3 + \boldsymbol{\Omega}\mathbf{e}_3) + \mathbf{t}_{3p}[(\mathbf{p} - \mathbf{g}^a) \otimes (\mathbf{g}^a - \mathbf{x}) \\ &\quad - (\mathbf{p} - \mathbf{g}^b) \otimes (\mathbf{g}^b - \mathbf{x})] \cdot (\operatorname{grad} \boldsymbol{\Omega}\mathbf{e}_3) \qquad (11)\\ \frac{1}{2}\mathbf{M}_p \cdot \boldsymbol{\Omega}_p &= \int_I (\mathbf{t}(\boldsymbol{\xi}) \otimes \mathbf{d}_p - \mathbf{d}_p \otimes \mathbf{t}(\boldsymbol{\xi})) \cdot (\operatorname{grad} \boldsymbol{\Omega})(\mathbf{g}^b - \mathbf{g}^a) \\ &= \frac{1}{2}\int_I (d_{3p}\bar{\mathbf{t}}(\boldsymbol{\xi}) - t_3(\boldsymbol{\xi})\bar{\mathbf{d}}_p) \otimes (\mathbf{g}^b - \mathbf{g}^a)(\operatorname{grad} \boldsymbol{\Omega}\mathbf{e}_3) \qquad (12)\end{aligned}$$

where the distance vector $\mathbf{d}_p$ can be written as $\mathbf{d}_p = \boldsymbol{\xi} - \mathbf{p}$. According to the previous notation $\mathbf{d}_p$ may be decomposed as $\mathbf{d}_p = \bar{\mathbf{d}}_p - \mathbf{d}_{3p}$.

For a chosen REV and a given class of regular motions, we impose that the mechanical power dissipated by the contact actions on $\mathscr{P}$ and $\mathscr{H}$ coincides. Under these assumptions, the membrane and moment tensors $\overline{\mathbf{N}}$ and $\mathbf{M}$, as well as plate shear vector $\mathbf{T}$ ($\mathbf{T} = \mathbf{N}\mathbf{e}_3$), may be expressed as a function of the vector $\mathbf{t}_p$, i.e. of the measure of the stress in the micro-mechanical model

$$\begin{aligned}\overline{\mathbf{N}} &= \frac{1}{2A}\sum_n \operatorname{sym} \bar{\mathbf{t}}_p \otimes (\mathbf{g}^b - \mathbf{g}^a)\\ \mathbf{T} &= \frac{1}{2A}\sum_n \mathbf{t}_{3p}(\mathbf{g}^b - \mathbf{g}^a)\\ \mathbf{M} &= \frac{1}{2A}\left[\sum_n \mathbf{t}_{3p}\operatorname{sym}[(\mathbf{p} - \mathbf{g}^a) \otimes (\mathbf{g}^a - \mathbf{x}) - (\mathbf{p} - \mathbf{g}^b) \otimes (\mathbf{g}^b - \mathbf{x})] + \sum_n \int_I \operatorname{sym}[d_{3p}\bar{\mathbf{t}}(\boldsymbol{\xi}) - t_3(\boldsymbol{\xi})\bar{\mathbf{d}}_p] \otimes (\mathbf{g}^b - \mathbf{g}^a)\right]\end{aligned} \qquad (13)$$

where A, Fig. 1, is the area of the chosen REV and the symbol $\sum$ indicates a summation extended to all the interfaces to which the chosen REV is in contact. It must be noted that the part of π associated to $\operatorname{skw}\{\operatorname{grad}\mathbf{W}\}$ and to $\operatorname{skw}\{\operatorname{grad}\mathbf{W}\mathbf{e}_3\}$ is not taken into account. In fact, in the adopted plate model these kinematic fields characterize neutral (rigid) motions.

The 1/2 coefficient which appears in the above expressions for $\mathbf{N}$, $\mathbf{T}$, and $\mathbf{M}$ depends on the fact that the power dissipated at the interface between a generic couple of blocks $(\mathscr{A}, \mathscr{B})$ involves both blocks.

2.4. The running bond case

In this section, the derivation of a plate model for running bond masonry is presented as a simple application of the proposed theory. The chosen REV is constituted by a single block. This means that (see Fig. 4), in order to evaluate expressions (13) four horizontal interfaces, $I_{-1,-1}$, $I_{+1,-1}$, $I_{+1,+1}$, $I_{-1,+1}$, and two vertical interfaces, $I_{2,0}$, $I_{-2,0}$, must be taken into account for the evaluation of the total internal power dissipated.

Let $\mathbf{g}_{i,j}$ be the position of the center of the generic brick in the 3D Euclidean space:

$$\mathbf{g}_{i,j} = i\frac{b}{2}\mathbf{e}_1 + ja\mathbf{e}_2 \qquad (14)$$

where b and a are brick length and brick height, respectively.

Due to the regularity of masonry under consideration, a $\mathbf{B}_{i,j}$ block interacts with a $\mathbf{B}_{i+k_1,j+k_2}$ block by means of I_{k_1,k_2} joint. In particular, it is worth noting that:

– if $k_1, k_2 = \pm 1$, then I_{k_1,k_2} represents a horizontal interface;
– if $k_1 = \pm 2$ and $k_2 = 0$, then I_{k_1,k_2} is a vertical interface.

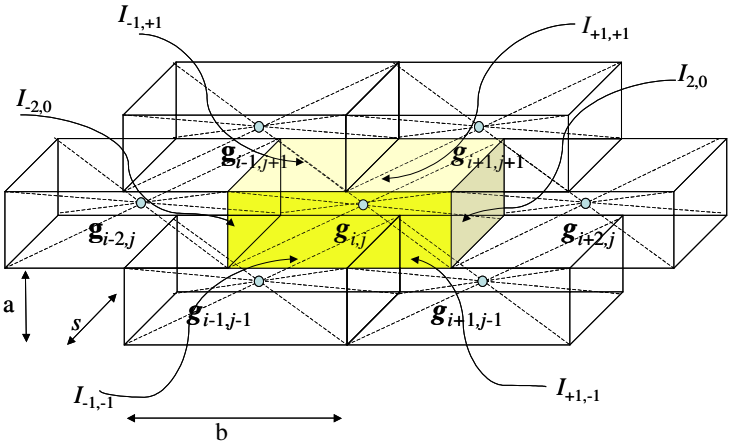

Fig. 4. Central brick infinitely resistant and mortar interfaces.

Hence, the jump of velocity between two adjacent blocks may be written in compact notation as follows:

$$[\mathbf{w}^{k_1,k_2}] = \Delta\mathbf{w}^{k_1,k_2} + \Delta\boldsymbol{\Omega}^{k_1,k_2}(\mathbf{g}^{i+k_1,j+k_2} - \mathbf{g}^{i,j}) \tag{15}$$

where

$$\begin{aligned}
\Delta w_1^{k_1,k_2} &= w_1^{i+k_1,j+k_2} - w_1^{k_1,k_2} + k_2 a\frac{\Omega_{21}^{i+k_1,j+k_2} + \Omega_{21}^{k_1,k_2}}{2}\\
\Delta w_2^{k_1,k_2} &= w_2^{i+k_1,j+k_2} - w_2^{k_1,k_2} - k_1\frac{b}{2}\frac{\Omega_{21}^{i+k_1,j+k_2} + \Omega_{21}^{k_1,k_2}}{2}\\
\Delta w_3^{k_1,k_2} &= w_3^{i+k_1,j+k_2} - w_3^{k_1,k_2} + k_1\frac{b}{2}\frac{\Omega_{32}^{i+k_1,j+k_2} + \Omega_{32}^{k_1,k_2}}{2} - k_2 a\frac{\Omega_{31}^{i+k_1,j+k_2} + \Omega_{31}^{k_1,k_2}}{2}\\
\Delta\Omega_{21}^{k_1,k_2} &= \Omega_{21}^{i+k_1,j+k_2} - \Omega_{21}^{k_1,k_2}\\
\Delta\Omega_{32}^{k_1,k_2} &= \Omega_{32}^{i+k_1,j+k_2} - \Omega_{32}^{k_1,k_2}\\
\Delta\Omega_{31}^{k_1,k_2} &= \Omega_{31}^{i+k_1,j+k_2} - \Omega_{31}^{k_1,k_2}
\end{aligned} \tag{16}$$

Eq. (16) provides the jumps of velocities on each interface, once constants k_1 and k_2 are suitably fixed.

According to Cecchi and Sab (2004) and Cecchi and Rizzi (2003) and starting from Eqs. (9) and (10), the identification between 3D discrete model and 2D continuum model has been obtained assuming:

$$\begin{aligned}
&\mathbf{w}^{i,j} = \mathbf{w}(\mathbf{g}^{i,j})\\
&\Omega_{32}^{i,j} = \omega_1(\mathbf{g}^{i,j})\\
&\Omega_{31}^{i,j} = -\omega_2(\mathbf{g}^{i,j})\\
&\Omega_{12}^{i,j} = 0.
\end{aligned} \tag{17}$$

It is worth noting that in the Reissner–Mindlin model proposed $\Omega_{12}^{i,j} = 0$, as shown in Eq. (17).

Fig. 5a shows the effect on the brickwork of a homogeneous deformation $\omega_{1,1} \neq 0$ with all the other strain measures set to zero. It must be noted that both head and bed joints are involved in the dissipation induced by this deformation. Fig. 5b shows the effect on the brickwork of a homogeneous deformation in which $\omega_{2,2} \neq 0$ and all the other strain measures are set to zero. In this case, it is interesting to note that only the bed joints present a relative jump of velocities between adjacent bricks.

Similarly, in Figs. 5c and d the cases $\omega_{1,2} \neq 0$ and $\omega_{2,1} \neq 0$ are examined. In the first case, no bending moment is present in the head joints, whereas there is torsion of the bed joints. On the contrary, in the second case, torsion is present in the head joints and bending moment acts in the bed joints.

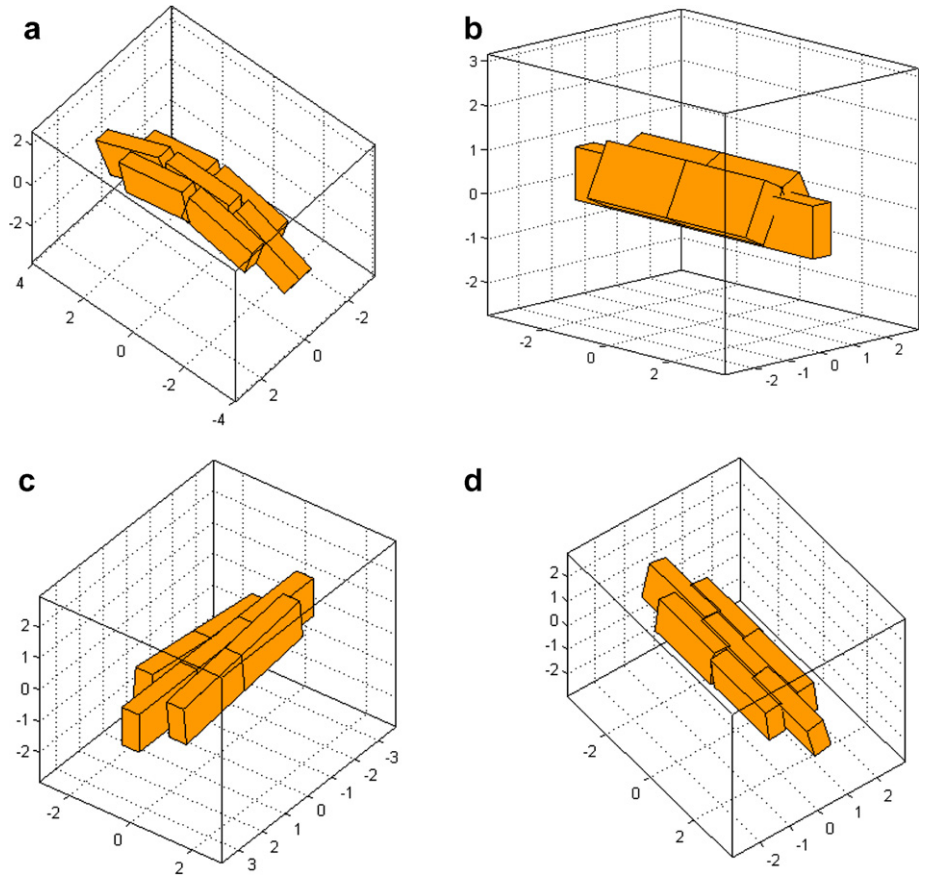

Fig. 5. Elementary homogeneous deformations applied to the representative volume element: (a) $\omega_{1,1} = \dot{\chi}_{11}$, (b) $\omega_{2,2} = \dot{\chi}_{22}$, (c) $\omega_{2,1}$, (d) $\omega_{1,2}$.

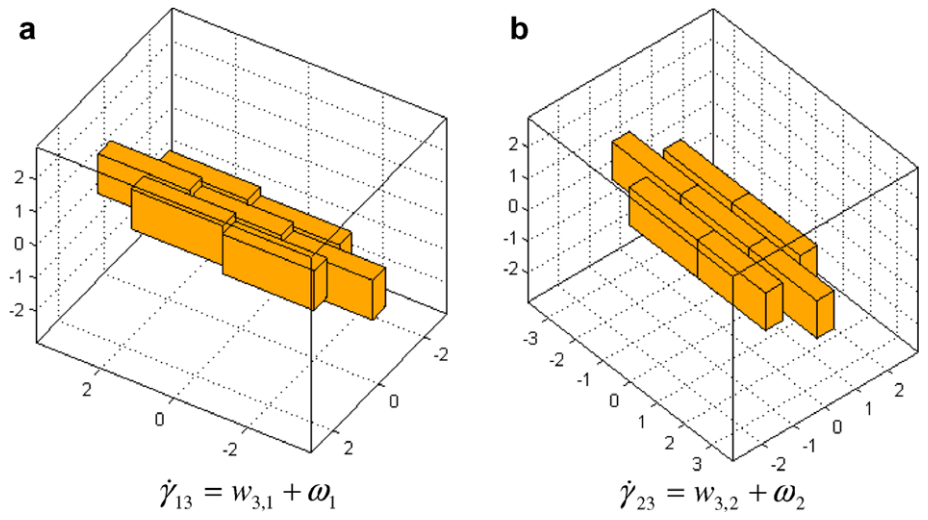

Fig. 6. Shear deformation rates: (a) $\dot{\gamma}_{13}$, (b) $\dot{\gamma}_{23}$.

Finally, Fig. 6 refers to the evaluation of the shear constants and shows shear deformation rates. In particular, Fig. 6a shows the $\dot{\gamma}_{13}$ component, while Fig. 6b the $\dot{\gamma}_{23}$ component.

3. Failure surfaces for Reissner–Mindlin periodic plates

In this section, a numerical procedure for obtaining macroscopic in- and out-of-plane failure surfaces for running bond masonry is presented. The procedure is developed under the hypotheses of Reissner–Mindlin plate theory, infinitely resistant bricks and joints both reduced to interfaces with a perfect plastic behavior and obeying an associated flow rule.

As it has been shown by Suquet (1983), macroscopic strength domains for periodic arrangements of heterogeneous materials can be obtained, in the framework of homogenization under the assumption of rigid-plastic behavior and associated flow rule for the constituent materials, by means of both static and kinematic theorems of limit analysis. Such approaches have been widely applied for the evaluation of both in-plane (de Buhan and de Felice, 1997; Milani et al., 2006a) and out-of-plane failure surfaces of masonry (Milani et al., 2006b; Sab, 2003), whereas, at present, there is a lack of literature, according to the authors' knowledge, concerning the derivation of the macroscopic failure surfaces for thick masonry panels.

On the other hand, experimental evidences show that sliding occurs in mortar joints with almost zero dilatancy with typical non-associated flow rule. This violates one of the hypotheses of classic limit analysis theory (see for instance Ferris and Tin-Loi, 2001; Orduña and Lourenço, 2005). This implies that the uniqueness of the ultimate load may be lost and a multiplicity of solutions can exist for limit analysis problems, as addressed for instance in Begg and Fishwick (1995).

On the contrary, classical limit analysis theorems assure the uniqueness of the ultimate load factor and lead to simple optimization problems. For the above reasons, in this section associated flow rules are assumed for the constituent materials.

In general, it is stressed that any non-linear failure criterion $\phi = \phi(\boldsymbol{\sigma})$ for joints can be assumed for the model at hand. As experimental evidences show, basic failure modes for masonry walls with weak mortar are a mixing of sliding along the joints (a), direct tensile splitting of the joints (b) and compressive crushing at the interface between mortar and bricks (c). These modes can be gathered adopting a Mohr–Coulomb failure criterion combined with tension cut-off and cap in compression, see Fig. 7, as suggested by Lourenço and Rots (1997).

Aiming at treating the problem in the framework of linear programming, within each interface I of area A^I, a piecewise linear approximation of the failure surface $\phi = \phi(\boldsymbol{\sigma})$ is adopted, constituted by n_{lin} planes of equation $\mathbf{A}_i^{I^T}\boldsymbol{\sigma} = c_i^I 1 \leqslant i \leqslant n_{\text{lin}}$, where $\boldsymbol{\sigma} = [\sigma_{33} \;\; \sigma_{13} \;\; \sigma_{23}]$, σ_{33} is the normal stress on the interface and σ_{13} and σ_{23} are tangential stresses along two assigned perpendicular directions, see Fig. 7.

Since the jump of velocity on interfaces is assumed to vary linearly in the discrete model (see Eq. (2)), for each interface $3 \cdot n_{\text{lin}}$ independent plastic multiplier rates are assumed as optimization variables.

In this way, for each interface I, the following equality constraints between plastic multiplier rates fields $\dot{\lambda}_i^I(\xi_1, \xi_2)$ and jump of velocity $[\mathbf{w}(\xi_1, \xi_2)]$ field on the interface are imposed:

$$[\mathbf{w}(\xi_1, \xi_2)] = \sum_{i=1}^{n_{\text{lin}}} \dot{\lambda}_i^I(\xi_1, \xi_2) \frac{\partial \phi}{\partial \boldsymbol{\sigma}} \tag{18}$$

where $\boldsymbol{\xi} = (\xi_1, \xi_2)$ is a local frame of reference laying on the interface plane and with axis ξ_3 orthogonal to the interface plane, see Fig. 7; $[\mathbf{w}(\xi_1, \xi_2)] = [\Delta w_{33} \;\; \Delta w_{13} \;\; \Delta w_{23}]^{\mathrm{T}}$ is the jump of velocity field (linear in (ξ_1, ξ_2)) on the Ith interface and Δw_{ij} corresponds to the jump along the direction i; $\dot{\lambda}_i^I(\xi_1, \xi_2)$ is the ith plastic multiplier rate field (linear in (ξ_1, ξ_2)) of the interface I, associated to the ith linearization plane of the failure surface.

It is worth noting that Eq. (18) is the specialization, for the interface I, of the well known normality rule $\dot{\varepsilon}_{ij} = \dot{\lambda}\frac{\partial \phi}{\partial \sigma_{ij}}$, where $\dot{\varepsilon}_{ij}$ is the plastic strain rate, $\dot{\lambda}$ is the plastic multiplier and ϕ is the failure surface, which coincides with the plastic potential in the case of associated plasticity.

In order to satisfy Eq. (18) for each point of the interface I, nine equality constraints for each interface have to be imposed, that corresponds to evaluate (18) in three different positions $P_k = (\xi_1^{P_k}, \xi_2^{P_k})$ on the interface I as follows:

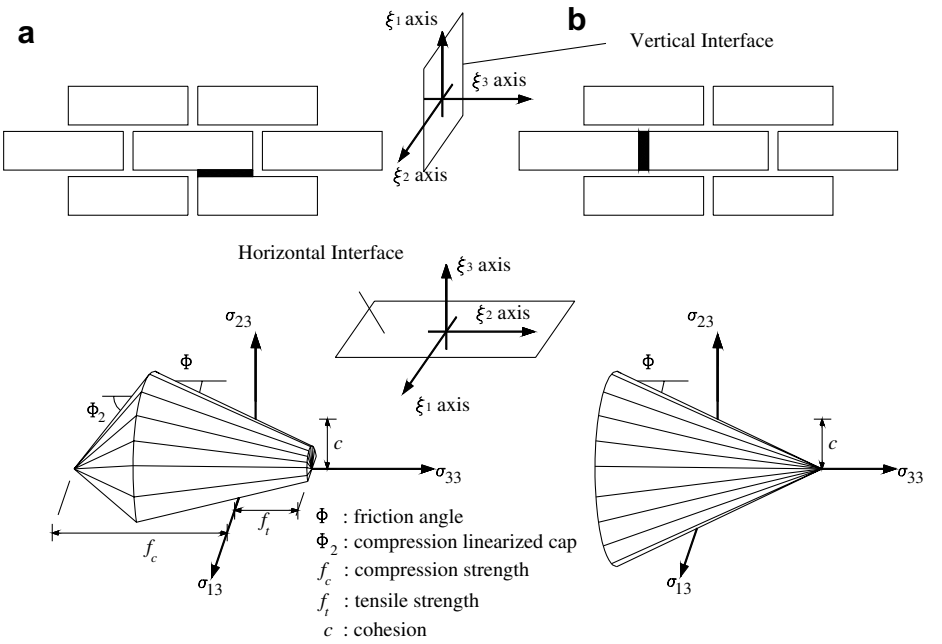

Fig. 7. Piecewise linear approximation of the failure criterion adopted for joints: (a) Mohr–Coulomb failure criterion with tension cut-off and linearized compression cap, (b) classic Mohr–Coulomb failure criterion.

$$[\mathbf{w}(\xi_1^{P_k}, \xi_2^{P_k})] = \sum_{i=1}^{n_{\text{lin}}} \dot{\lambda}_i^I(\xi_1^{P_k}, \xi_2^{P_k}) \frac{\partial \phi}{\partial \boldsymbol{\sigma}} \quad k = 1, 2, 3 \tag{19}$$

where $\dot{\lambda}_i^I(\xi_1^{P_k}, \xi_2^{P_k})$ is the is ith plastic multiplier rate of the interface I correspondent to $P_k = (\xi_1^{P_k}, \xi_2^{P_k})$.

Internal power dissipated on the Ith interface, defined as the product of the interface stress vector for the jump of velocities, is evaluated by means of the following equation:

$$\pi_{\text{int}}^I = \int_{A^I} [\mathbf{w}]^{\mathrm{T}} \boldsymbol{\sigma} \, \mathrm{d}A^I = \int_{A^I} \sum_{i=1}^{n_{\text{lin}}} \dot{\lambda}_i^I(\xi_1, \xi_2) \left[\frac{\partial \phi}{\partial \boldsymbol{\sigma}}\right]^{\mathrm{T}} \boldsymbol{\sigma} \, \mathrm{d}A^I = \frac{1}{3} \sum_{i=1}^{n_{\text{lin}}} c_i^I \sum_{k=1}^{3} \dot{\lambda}_i^I(\xi_1^{P_k}, \xi_2^{P_k}) A^I. \tag{20}$$

External power dissipated can be written as $\pi_{\text{ext}} = (\boldsymbol{\Sigma}_0^{\mathrm{T}} + \lambda \boldsymbol{\Sigma}_1^{\mathrm{T}})\mathbf{D}$, where $\boldsymbol{\Sigma}_0$ is the vector of permanent loads, λ is the load multiplier, $\boldsymbol{\Sigma}_1^{\mathrm{T}}$ is the vector of loads dependent on the load multiplier (i.e. the optimization direction in the space of macroscopic stresses) and $\mathbf{D}$ is the vector of macroscopic kinematic descriptors. $\mathbf{D}$ collects in-plane deformation rates $(\dot{E}_{11}\dot{E}_{12}\dot{E}_{22})$, out-of-plane deformation rates $(\dot{\chi}_{11}\dot{\chi}_{12}\dot{\chi}_{22})$ and shear deformation rates $(\dot{\gamma}_{13}\dot{\gamma}_{23})$, see Fig. 6. As the amplitude of the failure mechanism is arbitrary, a further normalization condition $\boldsymbol{\Sigma}_1^{\mathrm{T}}\mathbf{D} = 1$ is usually introduced. Hence, the external power becomes linear in $\mathbf{D}$ and λ and can be written as follows $\pi_{\text{ext}} = \boldsymbol{\Sigma}_0^{\mathrm{T}}\mathbf{D} + \lambda$.

Finally, from Eqs. (15) and (17), a linear relation between $\mathbf{D}$ and $[\mathbf{w}(\xi_1, \xi_2)]$ may be written for each interface I as follows:

$$[\mathbf{w}(\xi_1, \xi_2)] = \mathbf{G}^I(\xi_1, \xi_2)\mathbf{D} \tag{21}$$

where $\mathbf{G}^I(\xi_1, \xi_2)$ is a 3×10 matrix which depends only on the geometry of the interface under consideration (see Fig. 7).

Making use of both of Eqs. (18)–(21) and of the kinematic formulation of limit analysis, the following constrained minimization problem is finally obtained:

$$\begin{cases} \lambda = \min\limits_{\hat{\mathbf{x}}=[\mathbf{D}, \lambda_i^I(P_k)]} \sum\limits_{I=1}^{n^I} \pi_{\text{int}}^I - \boldsymbol{\Sigma}_0^{\mathrm{T}}\mathbf{D} \\ \boldsymbol{\Sigma}_1^{\mathrm{T}}\mathbf{D} = 1 \\ \mathbf{G}^I(P_k)\mathbf{D} = [\mathbf{w}(P_k)] = \sum\limits_{i=1}^{n_{\text{lin}}} \dot{\lambda}_i^I(\xi_1^{P_k}, \xi_2^{P_k}) \frac{\partial \phi}{\partial \boldsymbol{\sigma}} \quad P_k \in I \end{cases} \tag{22}$$

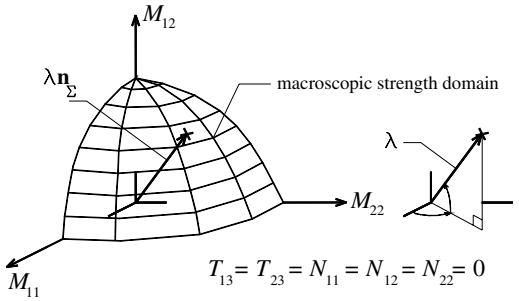

Fig. 8. Meaning of $\mathbf{n}_\Sigma$ in the special 3D case $\mathbf{\Sigma} = (M_{11}, M_{12}, M_{22})$.

where n^I is the total number of interfaces considered and $\hat{\mathbf{x}}$ is the vector of total optimization unknowns. It is stressed that the optimization problem given by Eq. (22) has been already treated in detail by Suquet (1983) in the general case and by some other authors in the past for obtaining in-plane homogenized failure surfaces for composites materials (see e.g Carvelli et al., 2000). In general, problem (22) can be easily handled numerically both by means of well know simplex and interior point methods, due to the very limited number of optimization unknowns involved. In fact, vector $\hat{\mathbf{x}}$ of global unknowns collects only $3 \cdot n_{\text{lin}} \cdot n^I$ plastic multiplier rates and macroscopic kinematic variables $\mathbf{D}$.

Problem (22) leads to reproduce the macroscopic combined in- and out-of-plane failure surfaces of masonry through a kinematic approach.

Denoting with $\hat{\Phi} = \hat{\Phi}(N_{11}, N_{12}, N_{22}, M_{11}, M_{12}, M_{22}, T_{13}, T_{23})$ the macroscopic failure polytope for masonry and with $\mathbf{\Sigma} = (N_{11}, N_{12}, N_{22}, M_{11}, M_{12}, M_{22}, T_{13}, T_{23})$, a 2D representation of $\hat{\Phi}$ with respect to variables Σ_i and Σ_j can be obtained fixing a direction versor $\mathbf{n}_\Sigma$ such that $[\mathbf{n}_\Sigma]^{\mathrm{T}} \mathbf{n}_k = 0 \ \forall k \neq i,j$, and solving the following optimization problem:

$$\begin{cases} \min\{\lambda\} = \sum_{I=1}^{n^I} \pi_{\text{int}}^I - \mathbf{\Sigma}_0^{\mathrm{T}} \mathbf{D} \\ \mathbf{n}_\Sigma^{\mathrm{T}} \mathbf{D} = 1 \quad \mathbf{n}_\Sigma^{\mathrm{T}} \mathbf{n}_k = 0 \quad \forall k \neq i,j \\ \mathbf{G}^I(P_k)\mathbf{D} = [\mathbf{w}(P_k)] = \sum_{i=1}^{n_{\text{lin}}} \dot{\lambda}_i^I(\xi_1^{P_k}, \xi_2^{P_k}) \frac{\partial \phi}{\partial \boldsymbol{\sigma}} \end{cases} \tag{23}$$

where λ represents the collapse load when a direction $\mathbf{n}_\Sigma$ in the $\mathbf{\Sigma}$ space (see Fig. 8) is assigned; $\mathbf{n}_k$ is a versor such that $\Sigma_k = \mathbf{\Sigma} \mathbf{n}_k$; i and j represent the axes of projection of $\hat{\Phi}$.

4. Failure surfaces

In this section, some cases of technical interest are discussed in detail, with the aim of testing both the reliability of the model proposed with respect to homogenized thin plate models presented in the technical literature (Sab, 2003; Milani et al., 2006b) and the influence of shear T_{13}–T_{23} macroscopic actions on the ultimate moments.

In the first example, Section 4.1, the influence of shear T_{13}–T_{23} macroscopic actions on the ultimate masonry horizontal bending, torsional and vertical bending moments (i.e. M_{11}, M_{12} and M_{22}) is addressed, see Fig. 9.

Two constitutive models are presented, assuming for joints both a classic Mohr–Coulomb (Model A) and a linearized Lourenço and Rots (1997) failure criterion (Model B). When a classic Mohr–Coulomb failure criterion is adopted, results obtained by Sab (2003) and Milani et al. (2006b) using a thin plate model are well reproduced by imposing $T_{13} = T_{23} = 0$. Two different vertical membrane loads N_{22} are applied and some sections M_{11}–M_{22} and M_{11}–M_{12} of the macroscopic failure polytope are reported varying T_{13} and T_{23}.

In the second example, Section 4.2, masonry considered by Page (1978) for performing experimental tests on a deep beam is considered. The relevant influence of vertical compressive membrane loads on M_{11}, M_{12} and M_{22} failure moments is addressed. As experimental evidences show, there is an optimal compressive load for

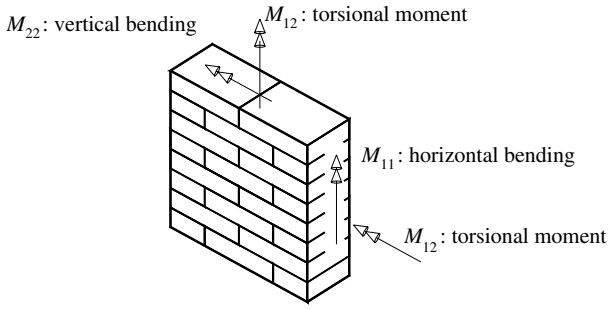

Fig. 9. Representation of horizontal bending moment M_{11}, vertical bending moment M_{22} and torsion M_{12}.

which failure moments reach a maximum. Exceeded this optimum point, out-of-plane strength begins to decrease until membrane compressive failure occurs. In particular, it is shown how a model with a classic Mohr–Coulomb failure criterion is incapable to reproduce this important phenomenon, whereas a model with limited compressive strength is able to better reproduce masonry behavior under combined in- and out-of-plane actions.

4.1. M_{11}–M_{12}–M_{22} failure polytope sections for different assigned T_{13}–T_{23}

In this section, standard Italian UNI bricks of dimensions $55 \times 120 \times 250$ mm^3 (height × thickness × length) and mortar joints reduced to interfaces with both a classic Mohr–Coulomb failure criterion (Model A) and a linearized Lourenço–Rots failure criterion (Model B) are assumed. Mechanical characteristics adopted for Model A and Model B are summarized in Table 1. It is worth noting that in Model B a very prominent shape ($\Phi_2 = 30°$) of the linearized compressive cap is assumed, Fig. 7. The goal of the comparison is to evaluate the influence of T_{13}–T_{23} on the macroscopic out-of-plane masonry failure surface in presence of different mechanical characteristics for mortar joints.

In Figs. 10 a and b, respectively, several sections M_{11}–M_{22} and M_{11}–M_{12} of the macroscopic failure polytope $\hat{\Phi}$ are reported for Model A varying T_{13} from zero to $T_{13} = T_{13}^f$, where T_{13}^f represents masonry failure when a pure T_{13} action is applied.

The same comparisons for Model A are illustrated in Figs. 11a and b varying T_{23} from zero to $T_{23} = T_{23}^f$.

As reported in Fig. 12a, the resultant failure surfaces correspond to that found by Sab (2003) and Milani et al. (2006b) with respectively kinematic and static Kirchhoff–Love models, assuming in the model proposed $T_{13} = T_{23} = 0$. Furthermore, it is worth noting that, when mortar friction angle is kept equal to zero, the well know square out-of-plane failure criterion proposed by Johansen for concrete slabs (1962) is reproduced, Fig. 12b.

It is worth noting that authors experienced no technically meaningful differences between Model A and Model B in absence of vertical membrane compressive load, as a consequence of the fact that out-of-plane failure is mostly related to tensile cracking. For this reason, here only Model A results are reported for $N_{22} = 0$.

On the contrary, significant differences occur between the models when a vertical membrane compressive load is applied. In Figs. 13a and b sections M_{11}–M_{22} and M_{11}–M_{12} of the masonry failure polytope $\hat{\Phi}$ are reported for Model A varying T_{13} and assuming $N_{22} = 30$ daN/mm. Let us remark that load bearing masonry

Table 1
Mechanical properties adopted for the numerical simulations (UNI bricks)

Model A – Mohr–Coulomb failure criterion		Model B – Linearized Lourenço and Rots (1997) failure criterion	
		c ($f_t = 1.7c$)	f_c
Φ	27°	0.132 (N/mm^2)	3.5 (N/mm^2)
		Φ	Φ_2
c	0.132 (N/mm^2)	27°	30°

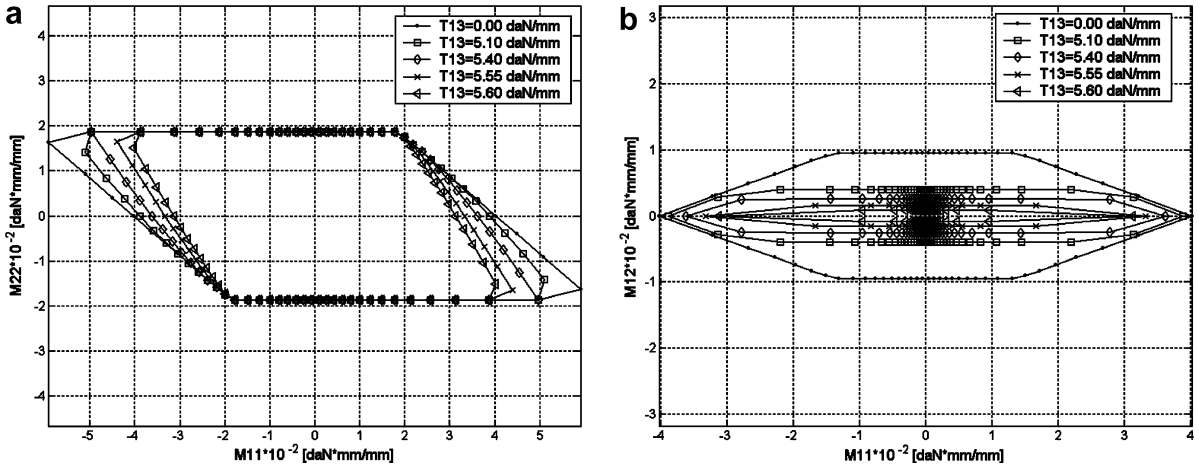

Fig. 10. Model A failure surface sections for different values of T_{13}: (a) M_{11}–M_{22} sections, (b) M_{11}–M_{12} sections.

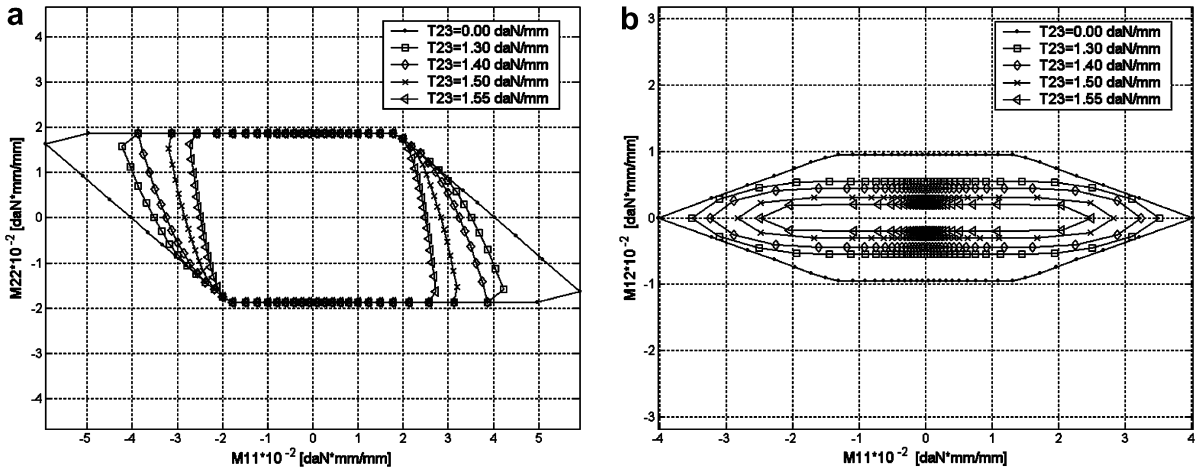

Fig. 11. Model A failure surface sections for different values of T_{23}: (a) M_{11}–M_{22} sections, (b) M_{11}–M_{12} sections.

walls are always subjected to relevant in-plane vertical compressive loads, due for instance by self weight and gravity loads of the floors.

In Figs. 13c and d the same results are reported adopting Model B. As can be noted by comparing the failure curves, technically meaningful differences occur between the models.

Finally, the results show that the macroscopic failure surface depends both on the geometrical and mechanical characteristics assumed for the components and that the proposed model is able to reproduce in a very simple manner the macroscopic strength domain whenever different failure behaviors for the components are taken into account.

4.2. Influence of the vertical compressive membrane load

The aim of this section is to show the influence of membrane compressive loads (kept constant) on the out-of-plane masonry failure surface.

The brickwork considered by Page (1978) for performing experimental tests on a deep beam (see also Sutcliffe et al., 2001, and Milani et al., 2006a) is considered. The units dimensions are $122 \times 37 \times 54$ mm^3, whereas the thickness of the mortar joints is 5 mm.

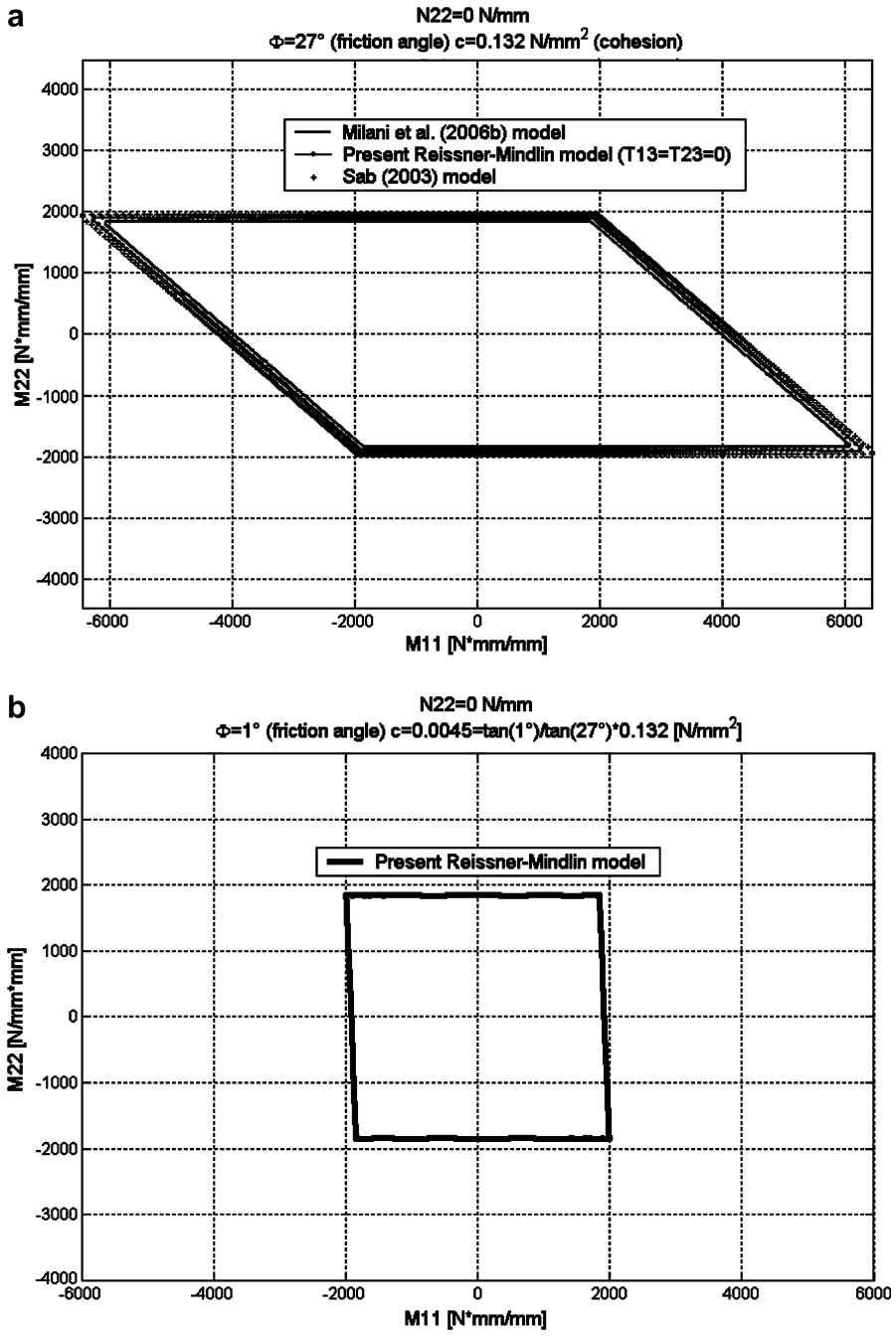

Fig. 12. (a) Comparison among the present model ($T_{13} = T_{23} = 0$), a Kirchhoff–Love kinematic model (Sab, 2003) and a Kirchhoff–Love static approach (Milani et al., 2006b), M_{11}–M_{22} failure surfaces. (b) Reproduction of Johansen model (1962) in case of friction angle equal to zero, M_{11}–M_{22} failure surfaces.

In the limit analysis here presented, as in the former case, joints are reduced to interfaces adopting for mortar both a classic Mohr–Coulomb failure surface (Model A) and a frictional-type failure surface with tensile and compressive cut-off (Model B).

Mechanical characteristics adopted for both models are summarized in Table 2.

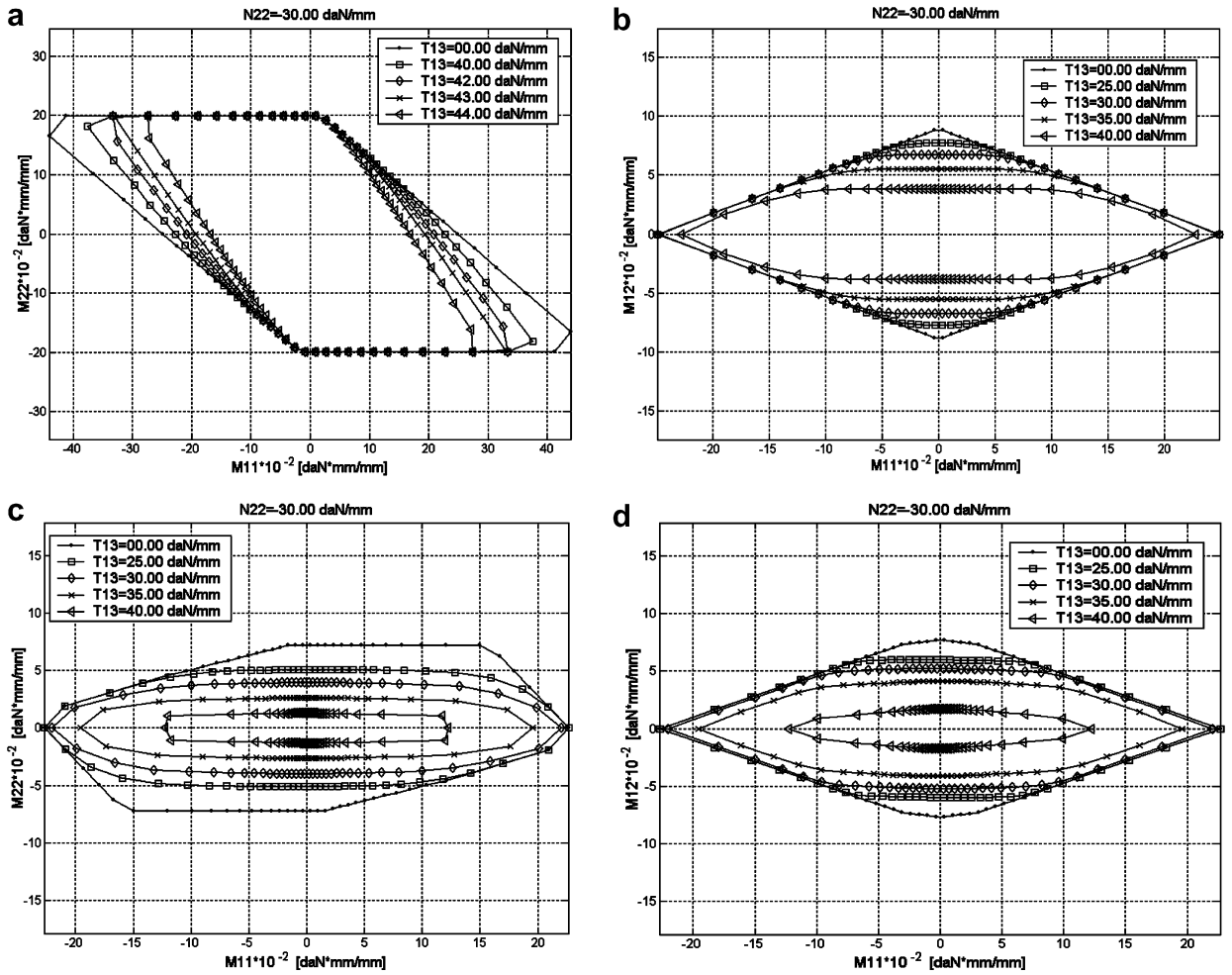

Fig. 13. (a) Model A, M_{11}–M_{22} failure surfaces at different values of T_{13}. (b) Model A, M_{11}–M_{12} failure surfaces at different values of T_{13}. (c) Model B, M_{11}–M_{22} failure surfaces at different values of T_{13}. (d) Model B, M_{11}–M_{12} failure surfaces at different values of T_{13}.

Table 2
Mechanical properties adopted for the numerical simulations, Page (1978) brickwork

Model A – Mohr–Coulomb failure criterion		Model B – Linearized Lourenço and Rots (1997) failure criterion	
		f_t ($c = 1.4 f_t$)	f_c
Φ	37°	0.29 (N/mm^2)	8.6 (N/mm^2)
		Φ	Φ_2
c	0.406 (N/mm^2)	37°	30°

In Figs. 14a and b, respectively, several sections M_{11}–M_{22} of the masonry failure polytope $\hat{\Phi}$ are reported for Model A and Model B respectively varying N_{22}.

In a similar way, in Figs. 14c and d the same simulations are reported representing sections M_{11}–M_{12}.

As it is possible to note, for both models vertical membrane load influences not only the horizontal bending moment but also the vertical one, as a consequence of the fact that also bed joints contribute to masonry vertical ultimate moment.

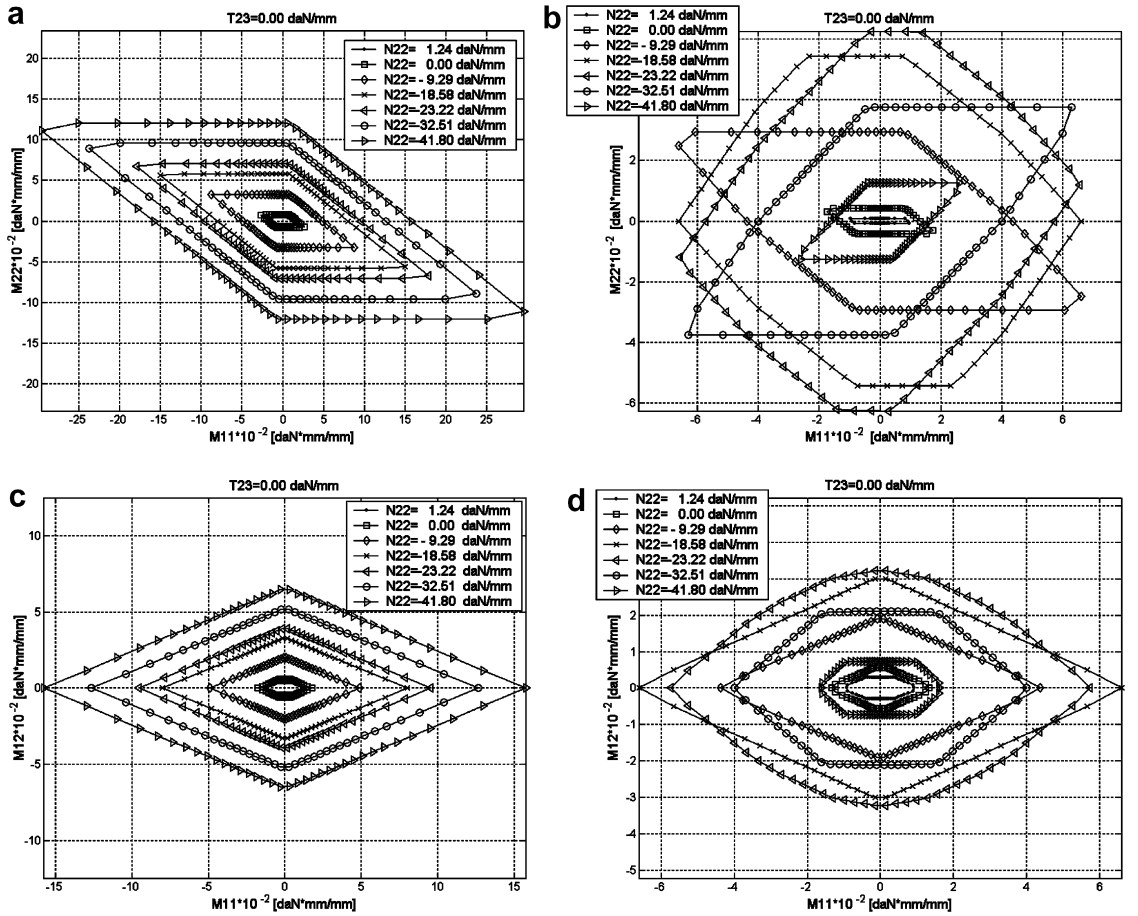

Fig. 14. (a) Model A, M_{11}–M_{22} failure surfaces at different values of N_{22}. (b) Model B, M_{11}–M_{22} failure surfaces at different values of N_{22}. (c) Model A, M_{11}–M_{12} failure surfaces at different values of N_{22}. (d) Model B, M_{11}–M_{12} failure surfaces at different values of N_{22}.

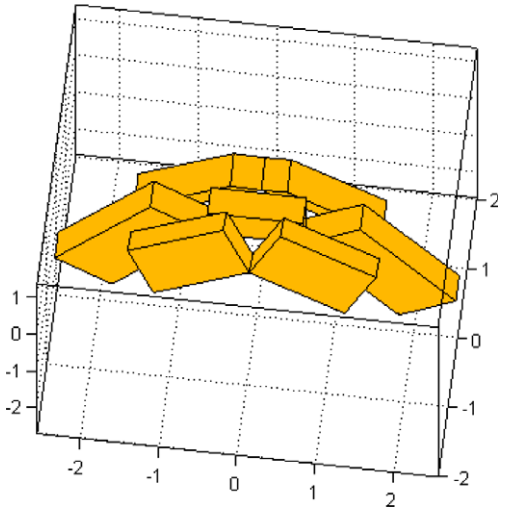

Fig. 15. Collapse mechanism for M_{11} failure bending moment in presence of a vertical compressive load and classic Mohr–Coulomb failure criterion for joints.

Furthermore, the relevant influence of a vertical compressive membrane load on M_{11}, M_{12} and M_{22} failure moments is worth noting.

A comparison between Figs. 14a and b shows how a classic Mohr–Coulomb failure criterion is incapable to reproduce the actual behavior of masonry under combined compressive membrane vertical loads and out-of-plane actions, whereas the phenomenon is kept by model B, which assumes a limited compressive strength for joints.

Obviously, this is due to the fact that a classic Mohr–Coulomb failure criterion does not provide compressive failure, as shown in Fig. 15, where the collapse mechanism for M_{11} failure bending moment is shown in presence of a vertical compressive load.

Finally, it is stressed that the choice of a failure criterion for joints with frictional behavior combined with a limited compressive and tensile strength is suitable for providing technically meaningful results in agreement with experimental evidences.

5. Structural examples

In this section, two structural examples of load bearing masonry walls out-of-plane loaded are analyzed, with the aim of comparing failure mechanisms and limit loads provided by the Reissner–Mindlin model at hand with the results obtained by means of a Kirchhoff–Love homogenized limit analysis approach.

5.1. Masonry wall subjected to cylindrical flexion (1D model)

A masonry wall, subjected to a horizontal distributed load depending on the load multiplier λ, Fig. 16, is considered. The panel is supposed clamped at the base whereas a simple support is disposed on the top. No lateral restraints are applied. As a consequence, the 2D brick plate model reduces to a 1D simply supported cantilever beam, where the only relevant internal actions are the vertical axial force N_{22}, the shear force T_{23} and the bending moment M_{22}. Blocks dimensions are assumed 20 cm × 10 cm (length × height) according to experimental data by Oliveira (2003) whereas masonry specific weight is assumed 2000 daN/m^3. The corresponding yield condition (N_{22}, T_{23}, M_{22}) can be formulated both analytically as a function of the wall thickness and mortar joint characteristics and resorting to numerical methods. On the other hand, the limit load for the structure can be evaluated making use both of manual calculations, being the horizontal reaction at the top of the wall the only redundant unknown or making use of a simple 1D FE kinematic limit analysis code. Here, the second approach is adopted. The panel is subdivided into a fixed number N_E of elements with $N_N = N_E + 1$ nodes, velocity field is assumed linear inside each element and possible jumps of velocities can occur between adjacent elements, see Fig. 16, as well as relative rotation rates. In this way, internal plastic dissipation π_I occurs only at an interface I between adjacent elements or on a boundary side, due to combined M_{22}–T_{23} actions. Vertical in-plane compressive load due to self weight is assumed to vary linearly from the top (zero) to the base (total weight of the wall).

Two panels of height $H = 300$ cm and different thickness (respectively $s = 30$ cm and $s = 60$ cm) are examined. A classic Mohr–Coulomb failure criterion is adopted for mortar joints reduced to interfaces, assuming a friction angle $\phi = 27°$ and cohesion $c = 0.1$ N/mm^2. 30 beam elements are used for the simulations, as shown in Figs. 16b and c, in order to have a reliable prediction of the actual position of plastic hinges.

In Fig. 17, failure mechanisms obtained using both the Reissner–Mindlin model proposed (a and b) and a Kirchhoff–Love model (c and d) are reported when panel thickness s is assumed respectively equal to 30 and 60 cm. As it possible to note, the influence of shear is particularly evident in the failure mechanism when $s = 60$ cm, with a percentage difference of the collapse load near 20%. On the contrary, when panel thickness is reduced to $s = 30$ cm, there are no technically meaningful differences between the two models.

5.2. Rectangular plate with central opening

The second example consists of a rectangular plate with central opening restrained at three edges and loaded with a distributed out-of-plane pressure.

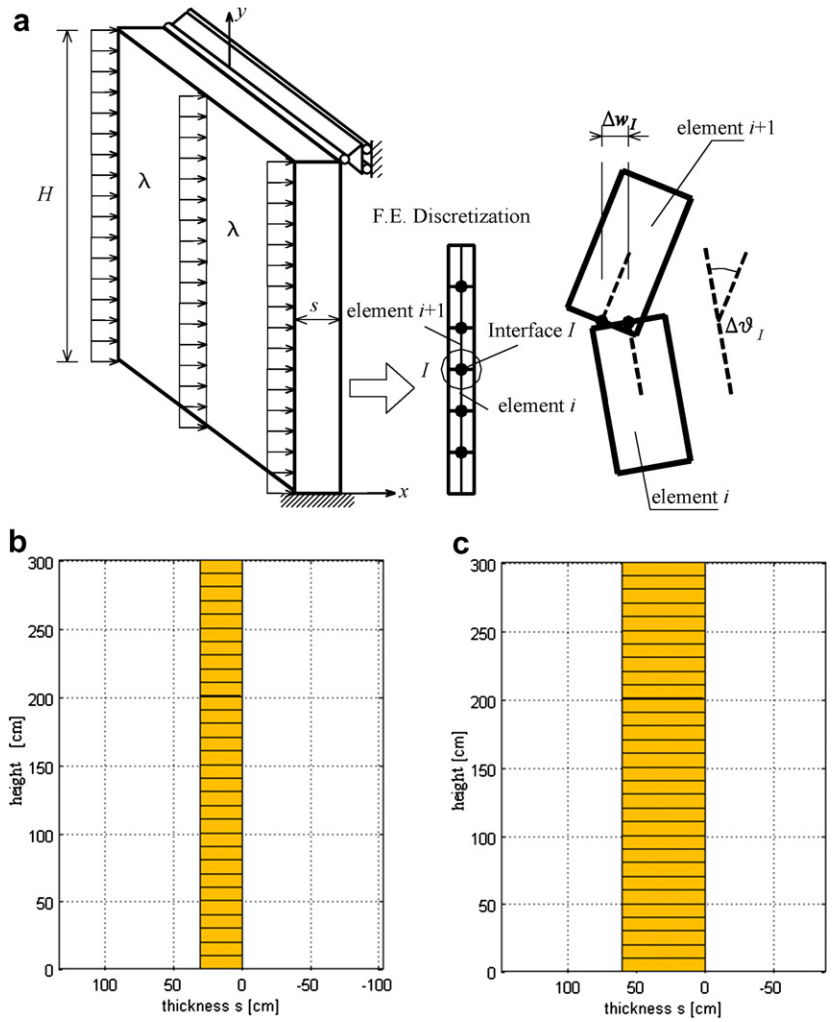

Fig. 16. Load bearing masonry wall: (a) geometry, (b) discretization with thickness $s = 30$ cm, (c) discretization with thickness $s = 60$ cm.

At this aim, a FE kinematic limit analysis code based on the Reissner–Mindlin plate hypotheses is used (Milani, 2006). It is worth noting that, at present, only few papers devoted to the study of this topic can be found in the technical literature (Capsoni and Corradi, 1999).

The FE formulation is based on a triangular discretization of a 2D domain. For each element E, one out-of-plane velocity unknown w_{zi}^{E} per node i is introduced, so that the velocity field is linear inside an element. Jumps of velocities can occur at the interface between adjacent triangles. Denoting with ϑ the angle between the interface and the x-axis, and with $\mathbf{n}$ and $\mathbf{t}$ the versors parallel and perpendicular to the interface direction, three different elementary interface plastic dissipations can occur, related respectively to shear T_{tz}, bending moment M_{nn} and torsion M_{nt}, as illustrated in Fig. 18. Following a general approach recently presented in the technical literature for the limit analysis of plane strain problems (Krabbenhoft et al., 2005), internal power dissipated is computed at each interface in terms of T_{tz}–M_{nn}–M_{nt} actions, once that both the in- and out-of-plane homogenized failure surfaces for masonry are provided.

The panel here analyzed originally was tested by Chong et al. (1994) and Southcombe et al. (1995). Its dimensions are 5615×2475 mm^2 and a central opening of dimensions 2260×1125 mm^2 is also present, as illustrated in Fig. 19. The wall was built in stretcher bond between two stiff abutments with the vertical edges simply supported (allowance for in-plane displacements was provided) and the top edge free. A completely restrained support was provided at the base because of practical difficulties in providing a simple support.

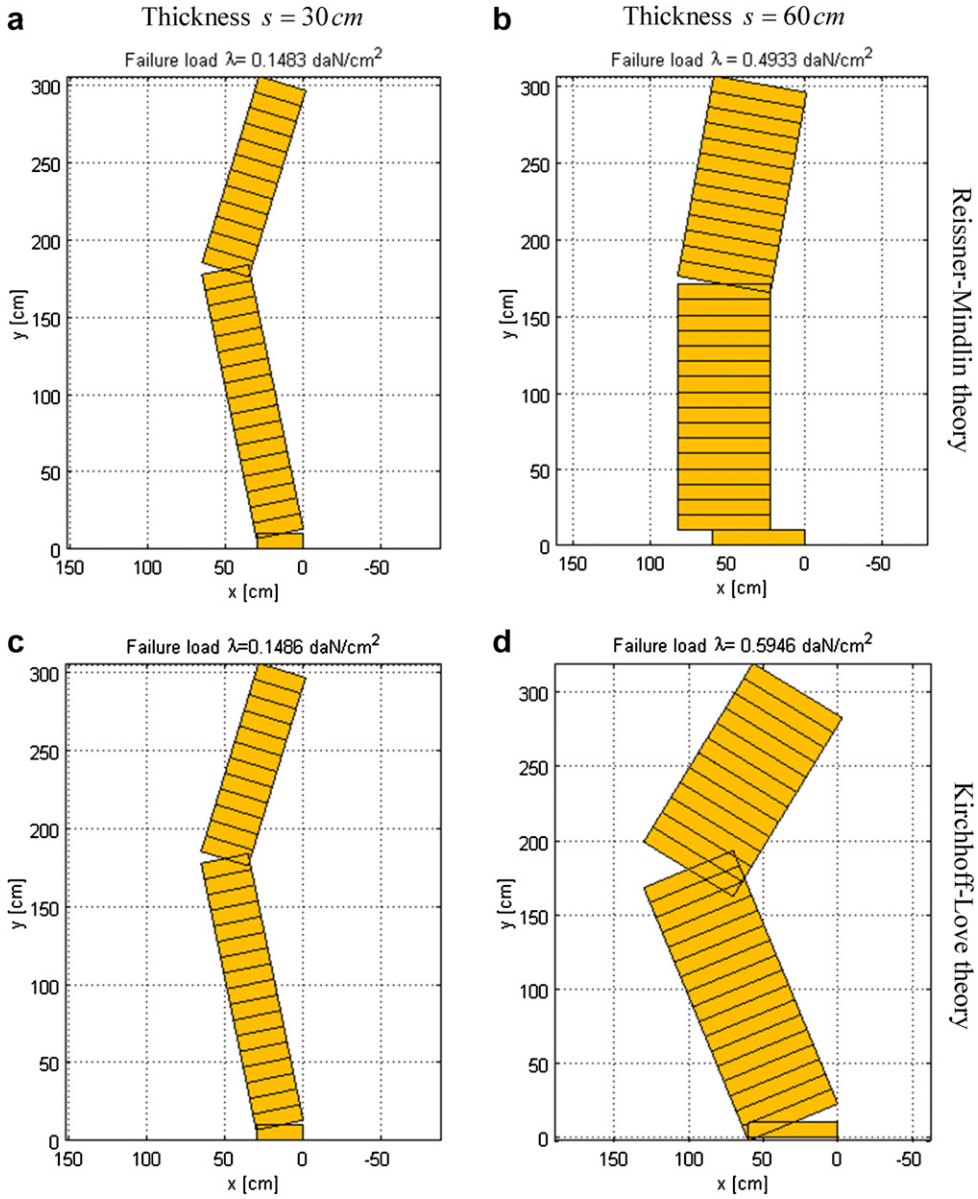

Fig. 17. Kinematic FE limit analysis: (a) wall thickness $s = 30$ cm and thick plate hypothesis, (b) wall thickness $s = 60$ cm and thick plate hypothesis, (c) wall thickness $s = 30$ cm and thin plate hypothesis, (d) wall thickness $s = 60$ cm and thin plate hypothesis.

The panel was loaded by air-bags until failure with an increasing out-of-plane uniform pressure p. The air pressure and the displacement d for the middle point of the free edge were monitored during testing. Wall thickness was $t_1 = 102$ mm. A full comparison between experimental data and a Kirchhoff–Love homogenized limit analysis approach is given in Milani et al. (2006b). In this section, in order to test the influence of shear on the ultimate out-of-plane pressure, a FE simulation is conducted with an augmented thickness $t_2 = 510\text{ mm} = 5t_1$, typical for ground floor masonry walls of historical buildings in Italian seismic area.

Mechanical properties at failure adopted for the mortar joints are given in Table 3 and are taken according to Chong et al. (1994) and Milani et al. (2006b).

Table 4 shows a comparison between the collapse loads obtained with the present Reissner–Mindlin FE model and a previously developed homogenized Kirchhoff–Love model (Milani et al., 2006b), assuming a wall thickness $t = t_1$ and $t = t_2$. As it is possible to note the difference between the failure loads so obtained is

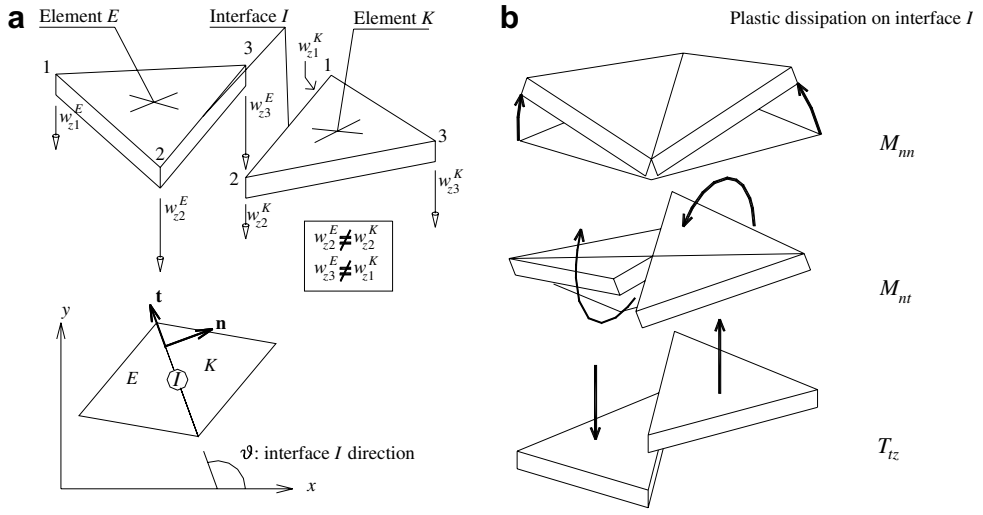

Fig. 18. Reissner–Mindlin FE kinematic limit analysis element: (a) field of velocities and discontinuity at each interface between adjacent triangles, (b) possible plastic dissipation at the interface due to bending moment, torsion and shear.

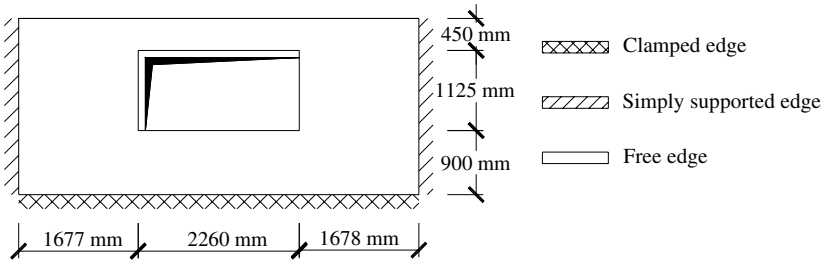

Fig. 19. Rectangular panel with central opening. Panel dimensions and boundary conditions.

Table 3
Rectangular panel with central opening. Mechanical characteristics assumed for mortar joints. Here f_t represents mortar tension cut-off; c is the mortar cohesion, Φ is the mortar friction angle, f_c is the compressive strength, Φ_2 is the shape of the linearized compressive cap

$f_t = 0.32\frac{N}{mm^2}$ (tension cut-off)
$c = 1 f_t$ (cohesion)
$\Phi = 36°$ (friction angle)
$f_c = 5\frac{N}{mm^2}$ (compressive strength)
$\Phi_2 = 90°$ (shape of the linearized compressive cap)

Table 4
Comparison between failure loads obtained using a Reissner–Mindlin FE limit analysis model and a Kirchhoff–Love FE limit analysis model, rectangular panel with central opening

Kirchhoff–Love model	Reissner–Mindlin model
Ultimate pressure (kN/m^2) $t = t_1 = 102.5$ *mm*[a]	
2.66[b]	2.65[b]
2.11	2.05
Ultimate pressure (kN/m^2) $t = t_2 = 5t_1$	
48.12	37.20

[a] Experimental collapse load value (Chong et al., 1994): 2.30.
[b] Munro and Da Fonseca (1978) yield-line method element.

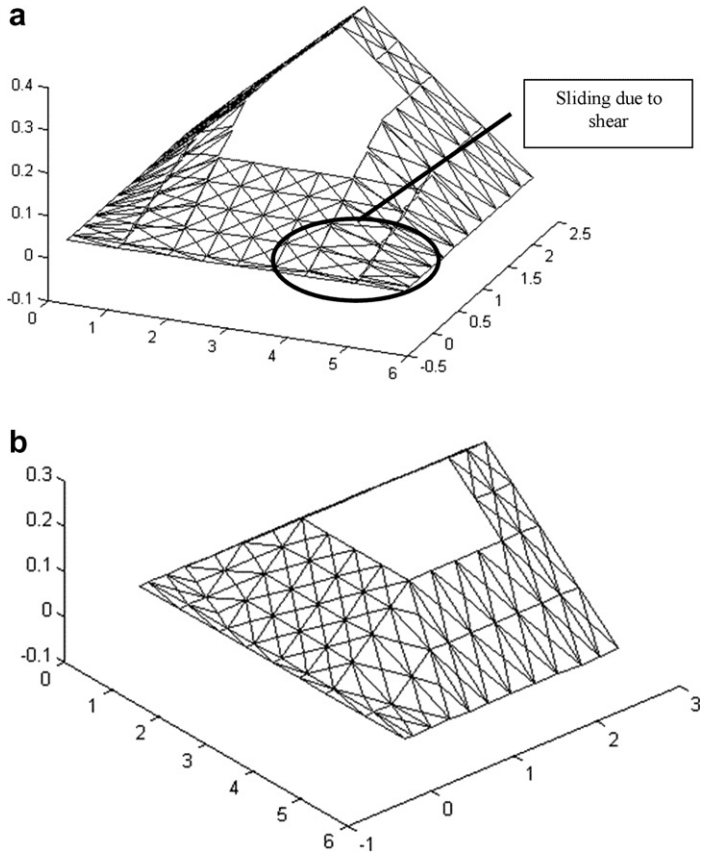

Fig. 20. Rectangular panel with central opening, thickness $t = t_2$. Deformed shape at collapse: (a) Reissner–Mindlin plate model, (b) Kirchhoff–Love plate model.

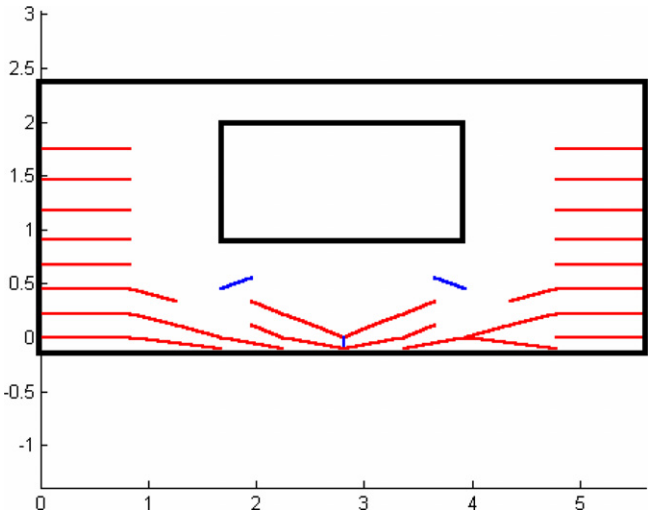

Fig. 21. Rectangular panel with central opening, thickness $t = t_2$. Plastic dissipation due to shear at the interface between adjacent triangles.

negligible when $t = t_1$, whereas is around 25% for $t = t_2$. A comparison between failure mechanisms provided by the two models when $t = t_2$, Fig. 20, confirms that shear effect is, in this case, important. In particular,

plastic dissipation due to T_{tz} is evident in correspondence of the bottom edges, as shown in Fig. 21, where shear plastic dissipation on the interfaces between adjacent triangles is reported.

6. Conclusions

A limit analysis model based on a compatible identification procedure has been presented for the study of out-of-plane loaded masonry walls under Reissner–Mindlin plate hypotheses. In the model, mortar joints are reduced to interfaces with frictional behavior with limited tensile and compressive strength, whereas bricks are supposed infinitely resistant.

Masonry failure polytopes can be easily provided with the model proposed in terms of membrane and plate actions, assuming different failure surfaces for joints. Several sections M_{11}–M_{22}, M_{11}–M_{12} of such polytopes are reported at different T_{13}, T_{23} and N_{22} values. Finally, the model is applied to two meaningful structural examples. The first concerns a masonry wall under cylindrical flexion, whereas the second consists of a rectangular plate with central opening out-of-plane loaded. For both cases, the influence of the shear strength on the collapse load is estimated varying panel slenderness. Finally, it is worth noting that the Reissner–Mindlin kinematic limit analysis model presented, differently from a classic Kirchhoff–Love approach, is able to reproduce, at a structural level, both rocking and sliding failures, two collapse mechanisms typical of masonry panels out-of-plane loaded.

Acknowledgments

A. Tralli and G. Milani gratefully acknowledge the support of the research project MIUR COFIN 2005 – Resistenza e degrado di interfacce in materiali e sistemi strutturali. Coordinator: Prof. A. Corigliano.

References

Begg, D., Fishwick, R., 1995. Numerical analysis of rigid block structures including sliding. In: Middleton, J., Pande, G. (Eds.), Computer Methods in Structural Masonry, vol. 3, pp. 177–183.

Capsoni, A., Corradi, L., 1999. Limit analysis of plates – a finite element formulation. Struct. Eng. Mech. 8, 325–341.

Carvelli, V., Maier, G., Taliercio, A., 2000. Kinematic limit analysis of periodic heterogeneous media. Comput. Model. Eng. Sci. 1 (2), 15–26.

Cecchi, A., Rizzi, N.L., 2003. Analisi in più parametri perturbativi per murature a struttura regolare: identificazione 3D con modelli 2D di piastra. In: Proc. XVI congresso AIMETA di meccanica teorica e applicata, Ferrara (Italy), 9–12 September.

Cecchi, A., Sab, K., 2004. A comparison between a 3D discrete model and two homogenised plate models for periodic elastic brickwork. Int. J. Solids Struct. 41 (9–10), 2259–2276.

Chong, V.L., Southcombe, C., May, I.M., 1994. The behaviour of laterally loaded masonry panels with openings. In: Proc. 3th Int. Masonry Conf., Proc. Brit. Mas. Soc., London, UK, pp. 178–182.

Corigliano, A., Maier, G., 1995. Dynamic shakedown analysis and bounds for elastoplastic structures with non associative, internal variable constitutive laws. Int. J. Solids Struct. 32 (21), 3145–3166.

de Buhan, P., de Felice, G., 1997. A homogenisation approach to the ultimate strength of brick masonry. J. Mech. Phys. Solids 45 (7), 1085–1104.

Del Piero, G., 1998. Limit analysis and no-tension materials. Int. J. Plasticity 14 (1–3), 259–271.

De Saxcé, G., Bousshine, L., 1998. Limit analysis theorems for implicit standard materials: application to the unilateral contact with dry friction and the non-associated flow rules in soils and rocks. Int. J. Mech. Sci. 40 (4), 387–398.

Ferris, M., Tin-Loi, F., 2001. Limit analysis of frictional block assemblies as a mathematical program with complementarity constraints. Int. J. Mech. Sci. 43, 209–224.

Gazzola, E.A., Drysdale, R.G., Essawy, A.S., 1985. Bending of concrete masonry walls at different angles to the bed joints. In: Proc. 3th North. Amer. Mas. Conf., Arlington, TX, USA, Paper 27.

Hill, R., 1965. A self-consistent mechanics of composites materials. J. Mech. Phys. Solids 13, 213–222.

Johansen, K.W., 1962. Yield-line Theory. Cement and Concrete Association, London.

Krabbenhoft, K., Lyamin, A.V., Hjiaj, M., Sloan, S.W., 2005. A new discontinuous upper bound limit analysis formulation. Int. J. Numer. Meth. Eng. 63, 1069–1088.

Lourenço, P.B., Rots, J., 1997. A multi-surface interface model for the analysis of masonry structures. J. Eng. Mech. ASCE 123 (7), 660–668.

Milani, G., 2006. A homogenized Reissner–Mindlin FE approach for the analysis at collapse of thick masonry walls out-of-plane loaded, in preparation.

Milani, G., Lourenço, P.B., Tralli, A., 2006a. Homogenised limit analysis of masonry walls. Part I: failure surfaces. Comput. Struct. 84 (3–4), 181–195.

Milani, G., Lourenço, P.B., Tralli, A., 2006b. Homogenization approach for the limit analysis of out-of-plane loaded masonry walls. J. Struct. Engrg. ASCE 132 (10), in press.

Munro, J., Da Fonseca, A.M.A., 1978. Yield-line method by finite elements and linear programming. J. Struct. Eng. ASCE B 56, 37–44.

Oliveira, D., 2003. Experimental and numerical analysis of block masonry structures under cyclic loading. Ph.D. Thesis, University of Minho, Portugal.

O.P.C.M. 3431/05 09/05/2005, 2005. Ulteriori modifiche ed integrazioni all'OPCM 3274/03 (in Italian) and O.P.C.M. 3274, 20/03/2003, Primi elementi in materia di criteri generali per la classificazione sismica del territorio nazionale e di normative tecniche per le costruzioni in zona sismica (in Italian).

Orduña, A., Lourenço, P.B., 2005. Three-dimensional limit analysis of rigid blocks assemblages. Part I: torsion failure on frictional joints and limit analysis formulation. Int. J. Solids Struct. 42 (18–19), 5140–5160.

Page, A.W., 1978. Finite element model for masonry. J. Struct. Div. ASCE 104 (8), 1267–1285.

Page, A.W., 1981. A biaxial failure criterion for brick masonry in the tension–tension range. Int. J. Masonry 1, 26–30.

Palmer, A.C., 1966. A limit theorem for materials with non-associated flow laws. J. Mecanique 5 (2), 217–222.

Sab, K., 2003. Yield design of thin periodic plates by a homogenisation technique and an application to masonry walls. C.R. Mechanique 331, 641–646.

Southcombe, C., May, I.M., Chong, V.L., 1995. The behaviour of brickwork panels with openings under lateral load. In: Proc. 4th Int. Masonry Conf., Proc. Brit. Mas. Soc., London, UK, vol. 1, pp. 105–110.

Spence, R., Coburn, A., 1992. Strengthening building of stone masonry to resist earthquakes. Meccanica 27, 213–221.

Suquet, P., 1983. Analyse limite et homogeneisation. Comp. Rendus Acad. Sci. – Series IIB – Mechanics 296, 1355–1358.

Sutcliffe, D.J., Yu, H.S., Page, A.W., 2001. Lower bound limit analysis of unreinforced masonry shear walls. Comput. Struct. 79, 1295–1312.